DOI: 10.13009/EUCASS2023-957
Aerospace Europe Conference 2023 – 10TH EUCASS – 9TH CEAS

Plasma testing of miniaturized Composite Overwrapped Pressure Vessels in reentry conditions

J. ElRassi[1⋆], *B. Helber*[1], *P. Schrooyen*[2], *A. Turchi*[4], *P. Jorge*[1], *T. Magin*[1], *L. Walpot*[3]
[1] *von Karman Institute, 1640 Rhode-Saint-Genese, Belgium*
[2] *Cenaero, 6041 Gosselies, Belgium*
[3] *European Space Agency, 2200 AG Noordwijk, Netherlands*
[4] *Italian Space Agency, Rome*
Joseph.elrassi@vki.ac.be · bernd.helber@vki.ac.be
⋆Corresponding author

Abstract

Composite Overwrapped Pressure Vessels (COPVs), made of a titanium liner and carbon fibre wrapping, are known to pose a certain risk for ground im pact as they are able to withstand the harsh reentry environment. Within an ESA project led by Cenaero, we designed and manufactured miniaturized COPVs in two configurations for high-enthalpy plasma tests in the VKI Plasmatron, presented in this paper.

The acquired experimental data included surface (pyrometer) and internal temperatures (type-K thermocouples), optical emission spectroscopy, high-quality photographs and movies. We were interested in the demise behaviour of the samples. During long-duration (>5 minutes) high-enthalpy tests, exceeding the actual reentry heat load, we achieved demise of the underlying titanium liner (burn-through). Main parts of the COPVs remained intact, such as the side- and backwalls.

1. Introduction

The rising space activities and the number of debris populating the low Earth orbits motivate the study of the atmospheric entry of those parts. In 2015, Klinkrad[1] estimated the amount of space debris orbiting the Earth larger than 10 cm to be around 34600 and an image of this increasing number of objects orbiting in low Earth orbit is shown in Fig. 1. The atmospheric drag will progressively slow these down and these will ultimately re-enter our atmosphere. According to Lips,[2] the current re-entry rate of man-made objects is about 400 tons per year. Since these are not designed to survive the harsh re-entry phase, most of them would be destroyed upon re-entry. Nonetheless, some survive the large heat flux applied during the uncontrolled re-entry and will crash on the ground threatening to cause some casualties. Therefore, one has to ensure that these will be destroyed upon re-entry and are not a risk to mankind.

During atmospheric entry, decommissioned spacecraft and satellite components are affected by aerodynamic heating due to the dissipation of a huge amount of kinetic energy into thermal energy. In these conditions, the vehicle usually breaks up into several parts which are, in turn, degraded by the high enthalpy flow. This can be observed in Fig. 2 (a) with the destructive atmospheric entry of the Automated Transfer Vehicle (ATV). Making use of the destructive reentry environment, the Design for Demise (D4D) solution is proposed at system design level by satellite manufacturers, ESA, and launch system providers to ensure compliance with risk requirements using passive, uncontrolled safe re-entry.[3]

This is a complex problem as the intrinsic nature of debris can be very different regarding the size and shape but also the material variety, which leads to difficulties regarding the identification and modelling of the phenomena involved in their destruction. Carbon Fibre Reinforced Polymer (CFRP) materials are a particular case since they are intrinsically similar to the basic ingredient for Thermal Protection System (TPS): carbon fibres and resin. Therefore, objects made with this type of material, for example, Composite Overwrapped Pressure Vessel (COPV) often survive the re-entry. Among many examples, the pressure vessel of the upper stage of the Vega launcher made its re-entry recently into Earth's atmosphere and hit almost intact on the ground in India (Fig. 2 (b)). Those spacecraft components are generally made of several layers of CFRP wrapped and bonded to the liner by a thin layer of adhesive.[4] The CFRP material undergoes physico-chemical processes during the reentry such as ablation, pyrolysis and spallation, which deteriorate its structure.

DOI: 10.13009/EUCASS2023-957

Figure 1: Human space debris orbiting the earth at low altitude (courtesy NASA).

(a) (b)

Figure 2: (a) Atmospheric reentry of ATV-4 observed from the international space station (Courtesy: ESA), (b) Vega first stage overwrapped pressurized tank, which landed in India on the 2 of November 2016.[5]

Within ESA's Clean Space initiative, a wide range of research programs has been funded with the intent of improving the understanding of spacecraft break-up and demise under uncontrolled Earth re-entry conditions. As part of the Belgian GSTP program "Identification of ablation process in porous materials" (ABLACCOD) awarded to Cenaero and VKI, we developed an experimental test campaign of miniaturized COPV samples for a better understanding of their demise phenomena and numerical simulations. The goal of this study was to obtain physical values that could be used in the development of adequate high-fidelity models, and in the long run allow for the design of material and components for destruction during atmospheric entry.

2. Material

Two test sample configurations have been designed for this project, a stagnation point and a sideways configuration Fig. 3. Both configurations are made up of a graphite and titanium liner wrapped by CFRP. Graphite is used as a structural liner, while grade-2 titanium is used for the area of interest (stagnation point: frontal hemisphere, sideways: central cylindrical tubing) to reassemble the actual COPV with titanium liner and wrapping. The wrapping has been by MOSS Composites (Belgium)[1]. Design and material information on the pressure vessel of the AVUM upper stage of the VEGA launcher have been extracted from Benton et al.[4] and from the manufacturer's website[2]. Three samples have been prepared for each configuration (six samples in total) with one sample for each configuration being made fully from a graphite liner (containing no titanium parts). The thickness of the titanium liner respects the thickness

[1] https://www.moss-composites.com/news-and-events?pgid=lgfm1up5-669aa010-52d8-409c-9208-a40b6d7c3b20
[2] https://www.northropgrumman.com/Capabilities/PressurantTanks/Pages/PressingTanksDataSheetsByPartNumber.aspx

DOI: 10.13009/EUCASS2023-957

of the full-scale tank (i.e., 0.8 mm). The fibres used to produce the CFRP sub-scale tanks are also corresponding to those used in the full-scale one. An epoxy resin with similar characteristics of the one use in the full-scale item (i.e., EPON-826) was used for the production of the model due to the unavailability of the EPON-826 on the European market. Special holding mechanisms have been developed for both configurations to allow proper clamping inside the wrapping machine. In the stagnation point configuration, this is done by holding the sample from the back. In the sideways configuration, it is held by the cross-bar. In both cases, the holding mechanisms were designed in a way to allow small enough wrapping angles as to fully close the stagnation point of the test samples. Each sample has been instrumented with four type-K thermocouples on the inside of the liner (inner side of the graphite/ titanium piece, Fig. 3).

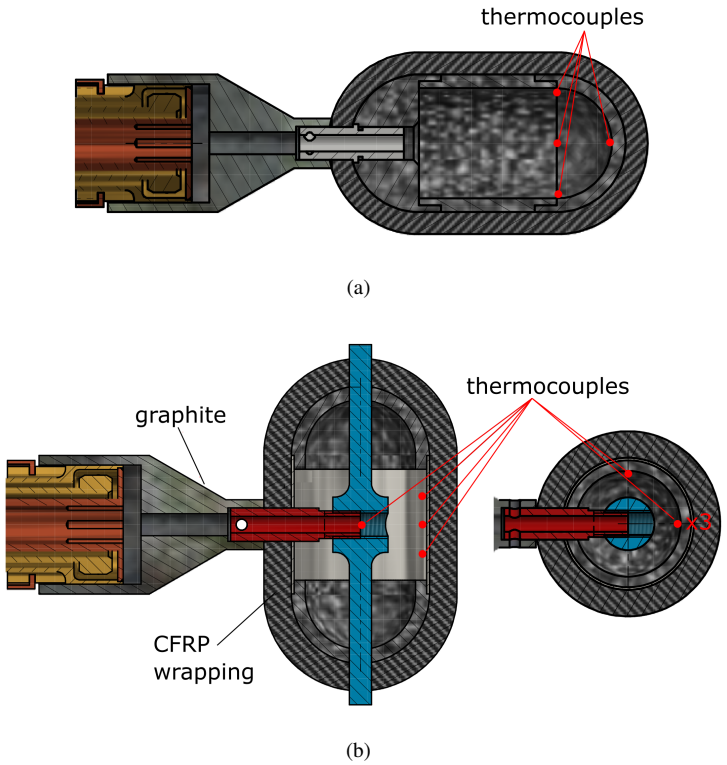

Figure 3: Test sample configuration: a) stagnation point with graphite or titanium frontal hemisphere; b) sideways with graphite or titanium inner tube; the graphite holder forms the connection to the water-cooled holding stem. The four type-K thermocouple locations are indicated.

3. Experimental Setup

3.1 Plasmatron Facility

This section reviews the Plasmatron facility as well as the associated measurement techniques applied during this test campaign. The Plasmatron facility Fig. 4 is a high enthalpy wind tunnel in which plasma is generated by electromagnetic induction and blown in the form of a jet inside a test chamber at sub-atmospheric pressure (between 10 mbar and 400 mbar).[6] The facility, which is the most powerful induction-coupled plasma (ICP) wind tunnel in the world, uses a high frequency, high power, high voltage (400 kHz, 1.20 MW, 2 kV) solid state (MOS technology) generator, feeding the single-turn inductor of the 160 mm diameter plasma torch. The torch is mounted on a 1.40 m diameter, 2.50 m long, water-cooled test chamber, fitted with different portholes that allow unrestricted optical access to the test section. Hot gas from the test chamber exits through a 700 kW heat exchanger to a group of three screw vacuum pumps and roots pumps. The closed-loop cooling system uses deionized water(2090 l/min) and fan-driven air coolers provide cooling to all facility components. The facility is computer controlled using a 719 I/O lines PLC, and two PCs for controlling and monitoring the Plasmatron operation. The test gas mass flow rate supplied to the torch is monitored through a calibrated gas rotameter (Bronkhorst EL-Flow F-203AV).

DOI: 10.13009/EUCASS2023-957

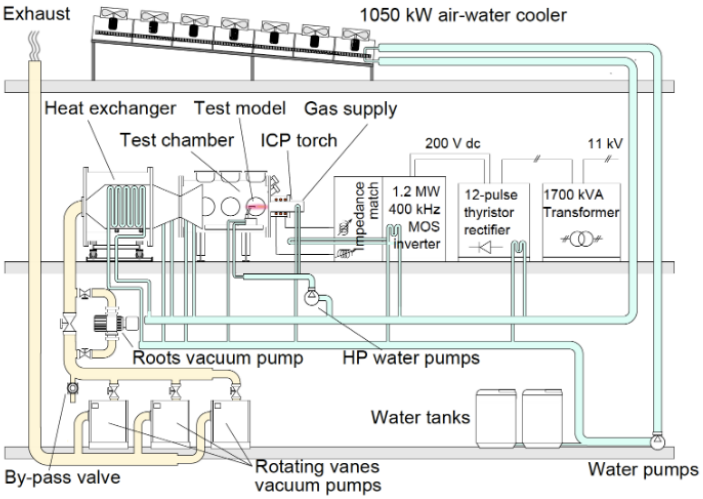

Figure 4: Overview of the VKI Plasmatron facility including cooling and vacuum circuits.

Before injection of a test sample, the plasma free-stream properties must be correctly adjusted and characterized. This procedure takes up to several minutes and any test sample positioned unprotected beside the hot plasma flow may heat up during this operation. Ablative materials based on resin impregnation experience degradation by pyrolysis of the resin at elevated temperatures, resulting in mass loss of the test sample. Such early material decomposition falsifies the test results regarding the material response and has to be avoided. A water-cooled sample condition control system is mounted inside the Plasmatron test chamber to retain the test sample before injection into the plasma flow. Besides the controlled retention of test samples before plasma flow exposure, the tested sample can be retracted into the system after plasma exposure to avoid any undesired contamination by the cold air jet. This cold air jet is blown into the test chamber after test execution to vent the test chamber.

3.2 Intrusive plasma flow measurements and plasma freestream characterization

Before and/or after each experimental run, the plasma condition set in the Plasmatron test chamber can be characterized by two intrusive probes injected into the plasma stream. Those are a water-cooled calorimeter for measuring the heat flux level provided by the high-temperature gas, as well as a pitot pressure measurement from which the dynamic pressure is obtained. In addition, the test chamber hosts a static pressure port outside the flowfield in order to record the test chamber static pressure during the experiment. An overview of the test chamber and an illustrative photograph of a COPV demise experiment is given in Fig. 5.

A water-cooled ($\sim$ 350 K) copper calorimeter is used during the test to measure the stagnation-point cold-wall heat flux. It is placed in the centre of the front face of a copper water-cooled probe holder with hemispherical the shape of 25 mm radius. This is determined by measuring the mass flow (controlled by a Bronkhorst M14 coriolic mass flow meter) and the temperature difference in the cooling water supply and return lines. Two type-E thermocouples are used for these measurements. In order to have correct measurements (i.e., one-dimensional conduction through the copper thickness), the sidewalls of the calorimeter have to be adiabatic. Therefore a Teflon insulator is installed between the calorimeter and the wall of the probe.

3.2.1 Pressure measurements

The Plasmatron chamber is equipped with an absolute pressure transducer (Memberanovac DM 12, Leybold Vacuum, OC Oerlikon Corporation AG, Switzerland) that measures the static pressure with an accuracy of ± 0.7 hPa. As the plasma jet is low subsonic (Ma$\approx$0.1), the static pressure is assumed constant inside the chamber. Given that the static pressure measurement is affected by the performance and stability of the vacuum pumps of the facility, an accuracy of $\pm 2\%$ is obtained.

A pitot probe is used to perform dynamic pressure measurements at stagnation point configuration. The Pitot line is connected to a Validyne variable reluctance pressure transducer (DP-15, Validyne Engineering Corp., USA) and the output is amplified by a voltage demodulator (CD-15, Validyne Engineering Corp., USA). Both Validyne and amplifier are calibrated with a Betz water manometer, leading to an uncertainty of $\pm 0.2\%$ in dynamic pressure.

DOI: 10.13009/EUCASS2023-957

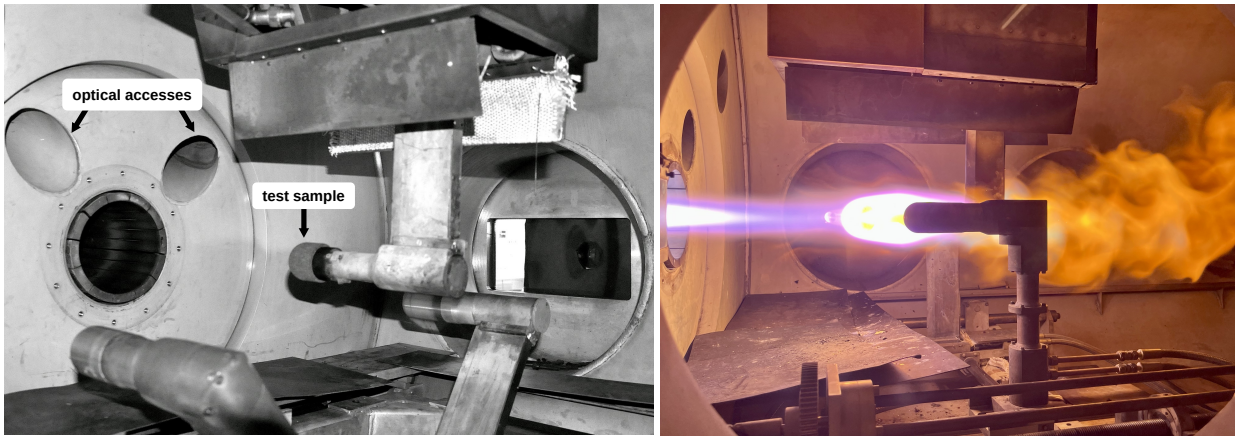

Figure 5: left: VKI Plasmatron test chamber overview presenting torch exit, (ablative) test sample extracted from retention system, two probe holders, optical accesses for pyrometer and HD-camera, and spectrometer optics access from side window; right: COPV sample demise test.

3.3 Non-Intrusive measurements

Following the introduction and characterization of the Plasmatron facility, this section reviews each measurement technique applied to the ablation tests. A comprehensive setup has been developed and applied to the facility for material response analysis. A schematic overview of the experimental techniques is given in Fig. 6, with each device being reviewed below.

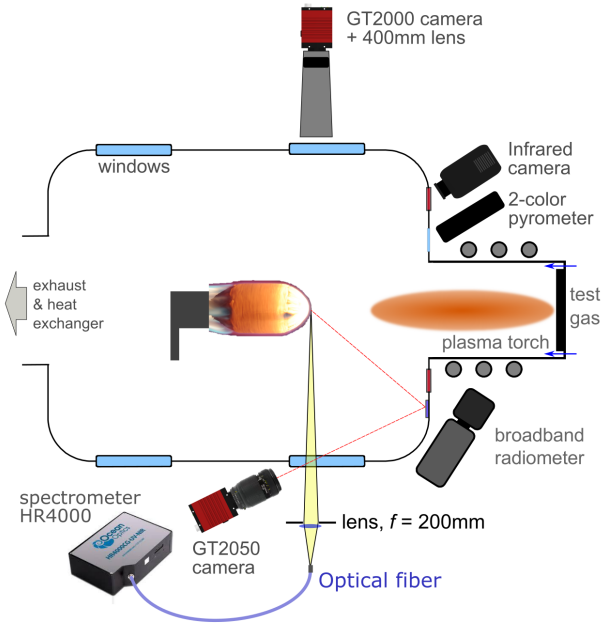

Figure 6: Experimental setup (non-intrusive instrumentation).

3.3.1 IR 2 color pyrometer

Two Raytek Marathon pyrometers are used to record the front surface (exposed to plasma) temperature of the sample. The instrument used for this study was a RM MR1SC series pyrometer with targeted temperature ranges between 1000 °C to 3000 °C.

The instrument measures over two overlapping narrow wavebands between 0.75-1.1µm, providing an output value independent on emissivity. It is pointed to the stagnation point of the sample.

DOI: 10.13009/EUCASS2023-957

A certified calibration of the MR1SC series pyrometer, 1000 °C to 3000 °C, has been carried out at the National Physical Laboratories in London. For this, a high-temperature graphite blackbody (estimated emissivity of 0.995) with an aperture of 25 mm diameter is used. The temperature of the blackbody is determined in terms of the International Temperature Scale of 1990 (ITS-90) using a calibrated linear pyrometer at wavelengths of nominally 650 nm and 900 nm. The measured distance from the back wall of the graphite blackbody to the front of the thermometer was 1000 mm. The instrument is then aligned and focused on the centre of the blackbody back wall. The calibration is performed using the supplied optical quartz window used at the Plasmatron test chamber. The window is placed nominally 10 mm in front of the Raytek thermometer and positioned so that the thermometer is aligned as closely as possible on the center of the window.

3.3.2 Radiometer

A broadband radiometer is used as an additional front surface temperature measurement device. The instrument is a special version of Heitronics IR-radiation-thermometer KT19.xx specifically designed for the VKI with a broad spectral range of 0.6-39 µm within a temperature range of 0 °C to 3000 °C. Applications of this type of IR radiometer are the estimation of material emissivities.

In operative Plasmatron conditions, a KRS-5 window, also known as thallium-bromoiodide (TlBr-TlI) is used along with the IR radiometer to provide optical access to the test chamber. This window enables measurements in the infrared range up to 40 µm. Such material is in fact one of the few existing crystals that offer about 70% transparency in the whole radiometer waveband. The raw IR radiometer output is the uncalibrated temperature evaluated from the measured radiance assuming an emissivity of 1. The IR radiometer was calibrated at the VKI using a LANDCAL R15 blackbody reference source together with the KRS-5 window in order to take the transmissivity into account.

3.3.3 Infrared surface temperature mapping

An infrared thermo-camera (FLIR A6750sc MWIR, FLIR SYSTEM, Hong Kong) with a thermal filter (ND3) is used to assess the temperature distribution over the probe and sample surfaces. It offers a resolution of 640×512 pixels and a maximum spectral sensitivity in the long-wavelength infrared range between 3 µm and 5 µm. The temperature range for the camera is 350 °C to 3000 °C. The camera is placed at 1 m distance from the probe, with an inclination of 47° with respect to the sample surface normal and optical access to the Plasmatron chamber is assured through a CaF2 window. Temperature uncertainties of the camera are ±1.5% considering also emissivity correction. The camera was calibrated together with the high-temperature ND3 filter by FLIR up to 3000 °C. To account for the proper line-of-sight transmissivity, the optical path encountered during the test conditions is reproduced. The calibration source is held at the same distance as the test probe w.r.t. the instrument and suitable windows are placed in front of the instrument lens.

3.3.4 High resolution cameras

Two high-resolution cameras were used to capture images during the test. A Prosilica GT2000 from the right side and a Prosilica GT2050 (2048 x 2048 CMOS sensor) from the left side. The GT2050 was focused on a mirror to capture the front of the front face of the sample while the GT2000 was aligned with the specimen from the side. The camera is designed for extreme environments with fast frame rates and fluctuating lighting conditions. It offers precise iris lens control allowing users to fix the aperture size to optimize depth of field, exposure, and gain without the need for additional control elements.

3.3.5 Emission Spectrometer

The COPV material samples have been produced with a high content of resin, which will lead to strong pyrolysis degradation during the experiment. Capturing the content of the pyrolysis outgassing is very challenging due to its highly transient behaviour and the mass loss of the sample through ablation at the same time. However, the pyrolysis progression is an interesting parameter for comparison to numerical models, such as the discontinuous Galerkin (DG) code ARGO, which combines fluid and material in one single domain. VKI has experience in investigating the pyrolysis loss from in-situ gas-phase measurements using optical spectrometers.[7] Those measurements can provide the time-varying signal of phenol-originated products, such H, CH, OH, NH, and C_2.

For this analysis, one low-resolution emission spectrometer was collimating the emission from the front of the COPV specimen during the experiments. This off-the-shelf Ocean Optics HR4000 spectrometer covers a wide spectral range (200 nm to 1000 nm) within one single acquisition and a minimum integration time of 5 ms. The light emitted by the plasma is collected through a variable aperture and focused by a plano-convex, uncoated fused silica lens on

DOI: 10.13009/EUCASS2023-957

the entry of one optical fibre (Ocean Optics QP600-2-SR/BX, 600±10 µm core diameter). The optical path is aligned perpendicular to the flow and tangential to the test sample surface.

All optical components operate in the HR4000 spectrometer wavelength range of 200 nm to 1100 nm. The fixed entrance slit width of 5 µm and a 300 grooves/mm grating typically leads to a resolution of approximately 0.7 nm (Full Width at Half Maximum (FWHM)), as can be determined using a low-pressure mercury (Hg) lamp (Oriel 6060), which provides a lower line broadening than covered by a single pixel of the Charge-Coupled Device (CCD) sensor ($\Delta\lambda_{\text{range}}/3648 \approx 0.22$ nm).

3.4 Test condition definition

For analysis of required test conditions, a reentry study in DRAMA[8] has been performed on hemispherical cylinders considering randomly tumbling as well as nose down and cross-flow configurations. The desired output of this analysis was the cold-wall heat fluxes, scaled to our ground-test probe shape, and total pressure along the debris trajectory for the different possible attitudes.

The COPV geometry is detailed in Table 1, where t_i is the thickness of component i. In DRAMA, there is no way to represent hemispheres, so spheres overlapping the cylinder body are created keeping the mass for the whole ensembly equal to the target one. The orbital parameters considered for the reentry are given in Table 2.

Table 1: Flight COPV geometric details

Cyl./Hem. radius [cm]	Cyl. length [cm]	Mass [kg]	t_{Liner} [cm]	t_{CFRP}[cm]
16.85	34.6	23	0.8	1

Table 2: Reentry orbit parameters

a [km]	e [−]	i [◦]	RAAN [◦]	ω [◦]	θ [◦]
7254.61	0.078677	69.48	305.92	44.73	185.55

The convective heating rate $\dot{Q}$ [W] of the evaluated geometry during the reentry is one of the main DRAMA outputs. However, DRAMA does not compute detailed information of the local heat flux over the whole structure, to then integrate over the surface. In order to get the stagnation-point heat flux of a cylinder, this procedure can be inverted, followed by the application of the relation between the stagnation heat flux of a sphere and a cone.

From the DRAMA calculation, several pairs of total pressure and stagnation heating can be picked while paying attention to the operational envelope of Plasmatron. In addition, given the small size of the ground-test samples, care should be taken to pick a reasonable heat flux to avoid demising the sample too quickly. For this reason, the average heat flux of the hole shape can be imposed instead of the stagnation point heat flux, translating into a conservative approach for design estimation. Generally, interesting trajectory points to choose are the maximum heat flux and the maximum dynamic pressure.

In the last step, one has to take into account that the available Plasmatron calorimeter is hemispherical and has a different radius than the hemispherical sample, and that the heat flux measured by the hemisphere will be different from the heat flux impinging on the sideways cylinder. For this reason, relations between different radius spheres under the same flow had to be found as well as relations between different shapes with the same radius. Several analytical solutions are available in the literature for the stagnation heat flux of both spheres and cylinders. These are based on similar solutions of the boundary layer with different sets of assumptions. The whole procedure will not be outlined here for conciseness and we only list the resulting test conditions for maximum heat flux in Table 3 below.

For the final test condition selection we chose the maximum heat flux in the tumbling case at the stagnation point of the hemisphere (3.54 MW/m^2) and the cylinder (3.08 MW/m2). We then increased the test time towards the full demise of the sample; and for the last test of each configuration raised the pressure to 200 hPa. The deviation in static test chamber pressure of 55 hPa from the computed 40 hPa was an outcome of an earlier test campaign on different test samples provided by EAST4D. For comparison purposes, we kept the same static pressure. Also, cold-wall heat fluxes for the stagnation point configuration were with 3.7 MW/m^2 slightly higher than targeted.

DOI: 10.13009/EUCASS2023-957

Table 3: Test matrix for maximum heat flux: Tumbling averaged over full surface, max. heat flux during tumbling at cylinder and hemisphere locations, and max. heat flux for fixed attitude.

		$\dot{q}_{max}$ [kW/m^2]	P_{tot} [hPa]	Testing time [s]	$\dot{q}_{cal}$ [kW/m^2]
Tumbling	total surface	378	40	141	483
Tumbling	Hemisphere	3234	40	94	3542
	Cylinder	2415	40	132	3084
Fixed Attitude	Hemisphere	4600	86	172	5040
	Cylinder	1948	25	132	2487

4. Results and Discussion

All tests were analysed to obtain surface and internal temperatures, however, one test from each configuration (run 6 and run 3) was chosen to be discussed in detail in this paper. Remarks, results and lessons learned, will be discussed briefly in further section for other tested samples.

4.1 Test matrix

The test matrix was chosen to replicate relative flight conditions. This analysis was completed from DRAMA's trajectory and aerothermal analysis for a previous test campaign done on the COPV samples. A total of six samples were tested in this campaign, three in the sideway configuration and three in the stagnation point configuration. For each configuration, one sample had a graphite liner while the other two had a titanium liner. Based on the computational analysis done in the previous campaign, the max heat flux condition was chosen, the stagnation and sideways samples were tested at 3.7 MW/m^2 and 3.1 MW/m^2, respectively. 55 Pa was chosen for static pressure to test one sample with graphite liner and one with titanium liner. Regarding test duration, one stagnation sample and one sideways sample, with titanium liner, were tested for a duration of 94 seconds and 133 seconds respectively. This duration was obtained from the trajectory analysis. The samples with graphite liner were tested with the same conditions (heat flux and pressure) until demise. The other sample with titanium liner was tested until demise as well but the pressure was increased to 200 Pa. For a better illustration of the test campaign, Table 4 summarizes the test conditions for all 6 samples tested in this experimental campaign.

Table 4: Test matrix including test run identifier, sample identifier (ending on 2 is sideways, ending on 1 is stagnation point), static test chamber pressure [hPa], electrical power [kW], cold-wall heat flux [MW/m^2], electrical torch power [kW], and test time [s].

Test	Sample ID	static pressure	Power	heat flux	test time
Run 1	2-2 (Ti liner)	55	430	3.7	94.2
Run 2	5-2 (graphite liner)	55	430	3.7	709.7
Run 3	1-2 (Ti liner)	200	334	3.7	291.1
Run 4	1-1 (Ti liner)	55	368	3.1	133.0
Run 5	5-1 (graphite liner)	55	370	3.1	285.9
Run 6	2-1 (Ti liner)	200	290	3.1	447.1

4.2 Test 3: Stagnation Configuration, 200 hPa, 3.7 MW/m^2, 291 s, demise.

All tests were analysed to obtain surface and internal temperatures along with optical images to highlight damage progression. However, one test from each configuration (run 3 (Stagnation) and run 6 (Sideways)) was chosen to be discussed in detail in this paper. Remarks, results and lessons learned will be compressed and discussed briefly further in Sec. 4.4 for other tested samples.

4.2.1 Test 3 Surface and internal temperature

Sample 3 with a titanium liner was subjected to 3.7 MW/m^2 heat flux. The sample was in stagnation configuration. The specimen was tested until demise.Fig. 7 (a) shows a picture of before and after the experiment for the tested

DOI: 10.13009/EUCASS2023-957

sample. It was apparent that after 295 seconds of testing, most of the frontal carbon wrapping had been removed and the titanium had changed colour due to its reaction with the plasma stream. The titanium liner did not survive the harsh environment at the stagnation point and a through hole was observed. Surface and internal temperature are plotted vs time (Fig. 7 (b)). The green line represents the temperature obtained by the pyrometer, the blue is the FLIR camera temperature ($\epsilon = 1$), the cyan is the radiometer temperature ($\epsilon = 1$), and the coloured lines below 1500 K are the four internal thermocouples.

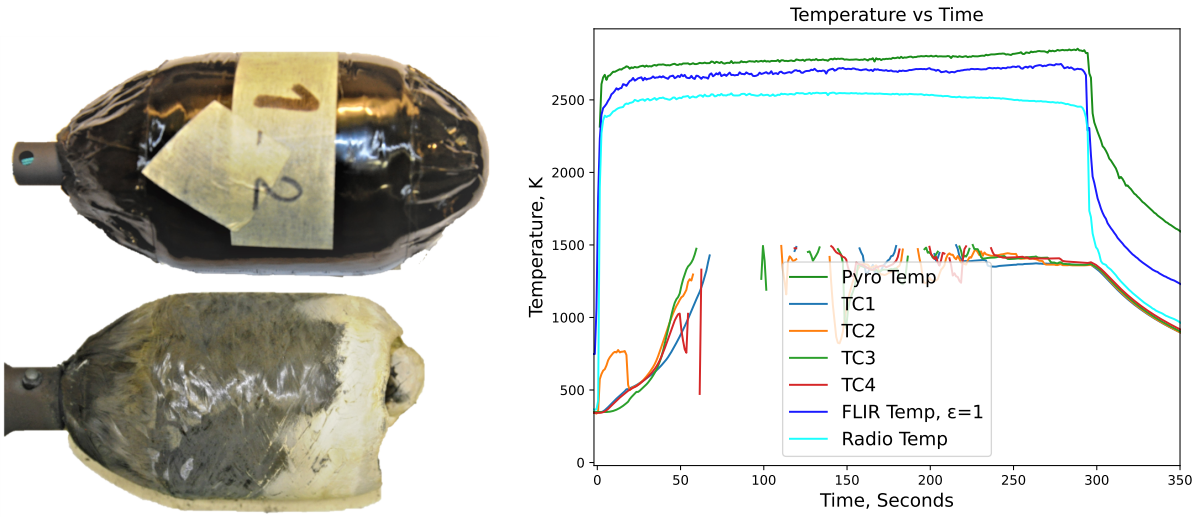

(a) (b)

Figure 7: Test 3 pre- and post-test photographs (a); surface and internal temperatures (b) (cut lines refer to thermocouple measurements beyond their temperature limit).

Regarding the surface temperature (Fig. 7), all instrumentation observed a similar behaviour: Upon inserting the specimen in the plasma stream, a sharp increase in temperature was observed, this was followed by a steady temperature until switching off the Plasmatron, where the temperature decreased rapidly. It was surprising that no sharp increase in temperature was observed after opening a hole in the specimen at the stagnation point, presumably, in stagnation point configuration, the oxidized layer on the inside Ti liner wall has similar T compared to what was monitored prior to opening a hole (front part uniform temperature including its demise). The thermocouple monitored a slower increase in temperature upon inserting the sample in the plasma stream compared to what was monitored on the surface, this indicates that the internal temperature is much lower than the surface temperature at the initial stages of the test. Type K thermocouples are rated for temperatures below 1500 K, after reaching the max temperature, the thermocouple were disconnected, noisy data was obtained, and data collected past that point is no longer reliable.

4.2.2 Test 3: Optical observation

The two optical cameras (GT2000 and GT2050) along with the FLIR images were used to observe the damage initiation, damage progression and failure (Fig. 8). The time was synchronized between all instrumentation and images were selected at a given time to highlight certain features. At 40 seconds (the initial surface temperature stabilization), most of the resin at the stagnation point was already burnt while some is still charring in the near-stagnation-regions. At 100 seconds into the test charring/ablation reached a steady state and no more resin was burning. As the test continues for another 200 seconds, carbon fibres started to degrade and rupture, ablation continues and reaches the titanium liner where the plasma melts it away and through hole is observed.

DOI: 10.13009/EUCASS2023-957

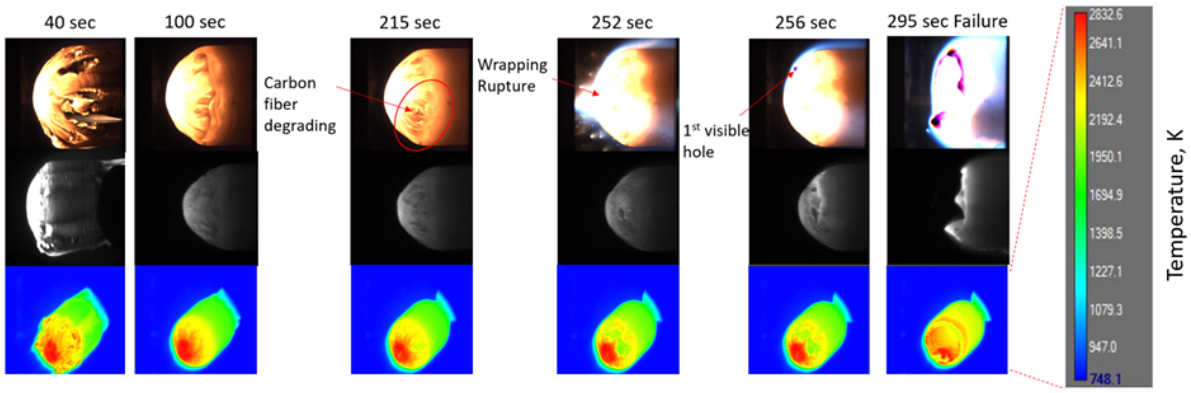

Figure 8: Test 3, damage progression vs time for frontal camera (GT2050), side camera (GT2000) and infrared camera.

4.2.3 Test 3: Gas-phase optical emission spectroscopy

The results from emission spectroscopy observation are provided below (Fig. 9) and show a strong signal of ablation contributors (CN violet), pyrolysis gases (NH and C_2 Swan), as well as metallic species towards the end of the experiment during demise (Ti). We are showing eight spectra taken during the whole experiment in two plots. The first plot highlights the start of the experiment, with strong CN and C_2 signals, followed by a decrease due to ablation and less pyrolysis outgassing. The second plot shows an increase in various lines over the whole spectrum after 260 seconds due to the demise process of the metallic liner.

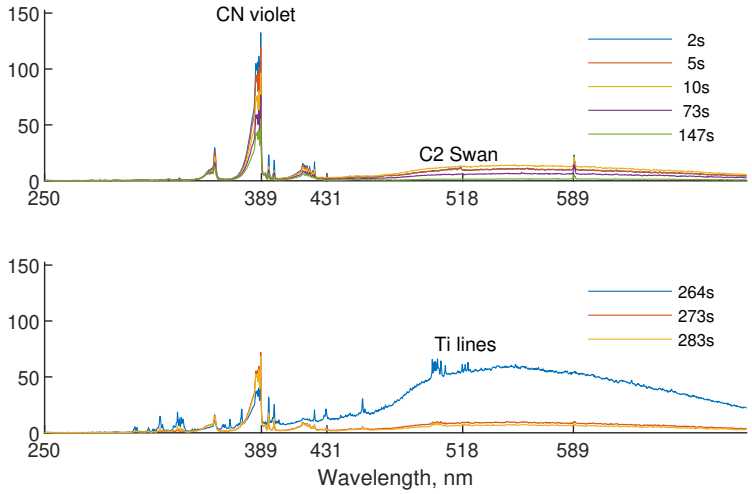

Figure 9: Test 3 emission spectrum overview clearly shows ablation species (CN violet) as well as transient species from the phenolic outgassing (C_2 Swan). Towards the end of the test, metallic species appear from the demise process (Ti), visible in the lower spectrum. The test time of each spectrum is indicated in the legend.

Time histories of those species show the temporal trend (Fig. 10), for example, the strong emission at the start of the experiment due to the extreme heating and strong pyrolysis outgassing. The time profiles are separated into three plots; first we show the whole test duration (Fig. 10 (a)), then the first 30 s (Fig. 10 (b)), followed by the last 40 s (Fig. 10 (c)). The emission decreases over test time as pyrolysis strongly progresses and also because the surface front moves away from the spectrometer optical path due to ablation. At 265 s a strong signal can be observed again due to the emission of metallic contributors, possibly coming from both, degeneration of the titanium liner but also from the internal thermocouples.

DOI: 10.13009/EUCASS2023-957

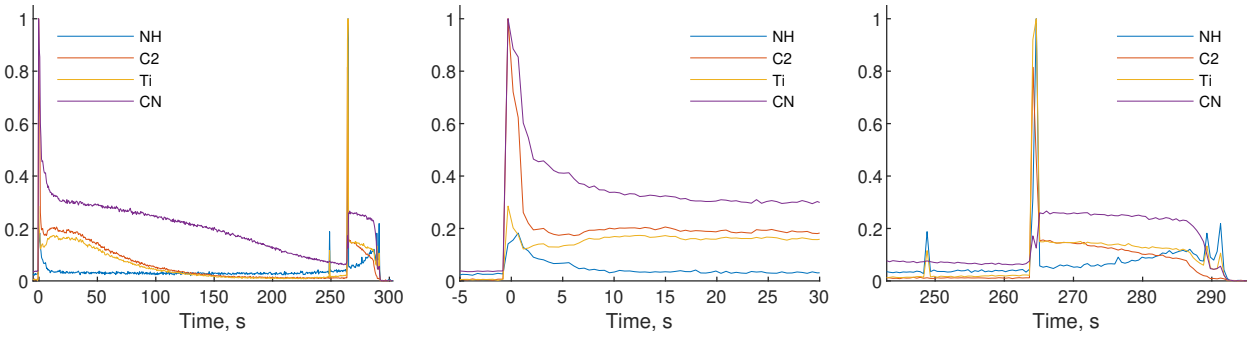

Figure 10: Test 3 temporal OES emission profiles over the whole test time (a), the first 30 s (b), and the last 40 s (c) show the strong emission at test start, mostly due to pyrolysis gas injection into the boundary layer, and the strong decrease during the test (a). Once the titanium liner starts demising, emission strongly rises again (c).

4.3 Test 6: Sideway configuration, 200 hPa, 3.1 MW/m^2, 447 s, demise.

4.3.1 Test 6 Surface and internal temperature

Test 6 with a titanium liner was subjected to 3.1 MW/m^2 heat flux. Unlike the previous sample, this sample was tested in a sideways configuration, creating a full 3D flowfield. The specimen was also tested until demise. Fig. 11 shows a picture of before and after the experiment for the tested sample. Internal and surface temperature had similar behaviour to test 3 (stagnation point), upon heating, a sharp increase in surface temperature was observed while the internal temperature, monitored with the thermocouple, increased gradually. The surface temperature stabilized after 60 seconds. At 400 sec a small decrease in surface temperature was observed (maily in FLIR and Radio data) and it was followed by a sharp increase. This behaviour is because the carbon wrapping degraded all the way and a hole opened in the liner material possibly causing the specimen to act as a blackbody cavity. This observation will be highlighted in further detail in the next section (Fig. 12).

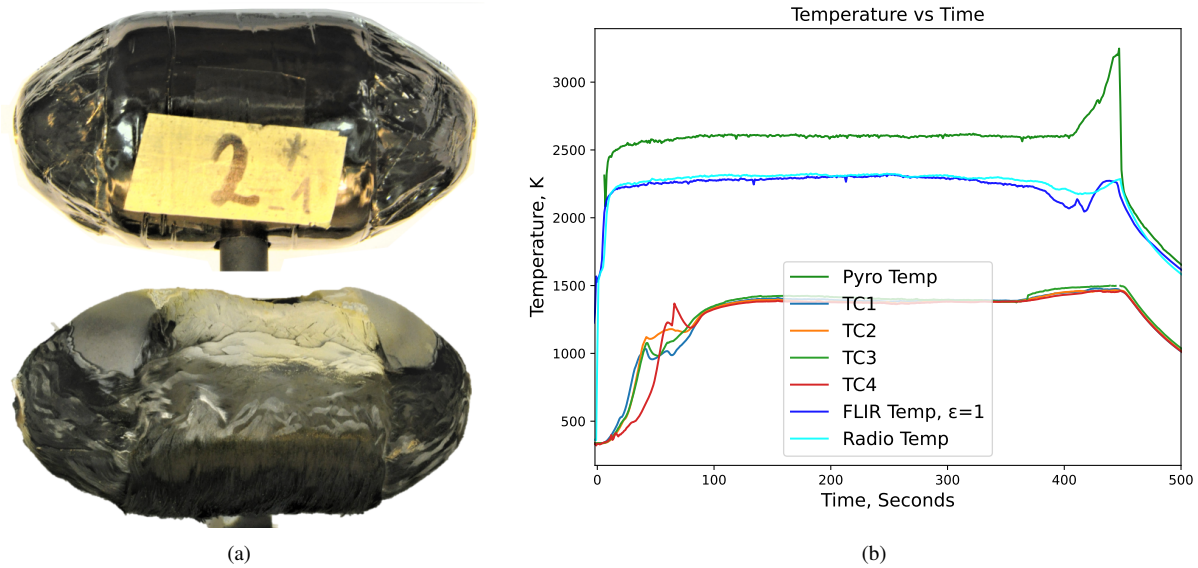

Figure 11: Pre- and post-test photographs for test 6 (a); surface and internal temperatures (b) (cut lines refer to thermocouple measurements beyond their temperature limit).

DOI: 10.13009/EUCASS2023-957

4.3.2 Test 6: Optical observation

The optical instrumentation was used to determine the carbon wrapping degradation as a function of time, similar to what was presented in test 3. The initial stage of damage was in the form of resin burning and charring of the carbon wrapping until a steady state ablation was reached (> 100 seconds). It was interesting to observe that the damage initiation was located between the face wrapping and the edge wrapping, this is highlighted in Fig. 12, 300 sec. This is likely due to a higher heatflux at the shoulder region of the sideways test sample compared to the stagnation point area. The higher heat flux in the shoulder region on flat-faced test samples has been discussed in detail by Fagnani.[9]

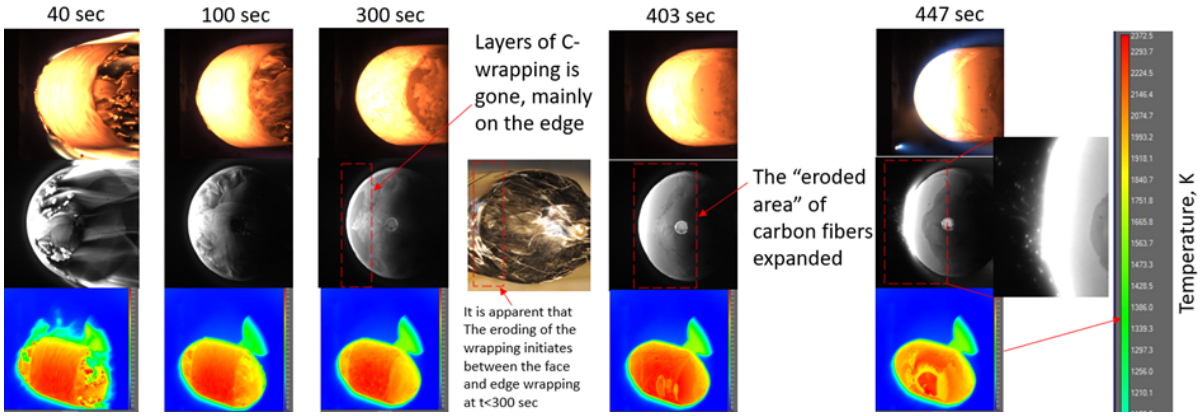

Figure 12: Test 6 damage progression vs time.

4.3.3 Test 6: Gas-phase optical emission spectroscopy

The results from emission spectroscopy observation are provided below (Fig. 13) and show again strong signals of ablation contributors (CN violet), pyrolysis gases (NH and C_2 Swan), as well as metallic species towards the end of the experiment during demise (Ti). We again show eight spectra taken during the whole experiment in two plots. The first plot highlights the start of the experiment, with strong CN and C_2 signals, followed by a decrease due to ablation and less pyrolysis outgassing. The second plot shows an increase in various lines over the whole spectrum after 421 seconds due to the demise process of the metallic liner, now even stronger than in the stagnation point test 3 reported above (Fig. 9). This can possibly be attributed to a larger boundary layer in the case of sideway configuration, thus, a larger integration volume of the emission spectrometer optics.

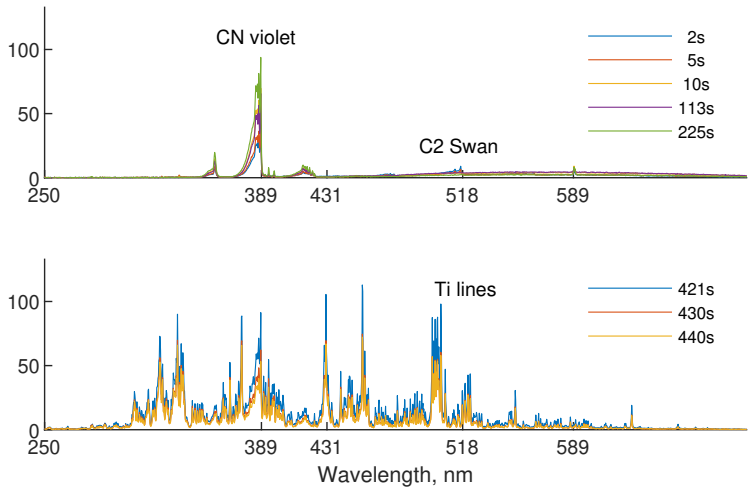

Figure 13: Test 6 emission spectrum overview clearly shows ablation species (CN violet) as well as transient species from the phenolic outgassing (C2 Swan). Towards the end of the test, metallic species appear from the demise process (Ti), visible in the lower spectrum. The test time of each spectrum is indicated in the legend.

Time histories of those species show the temporal trend (Fig. 10), for example, the strong emission at the start

DOI: 10.13009/EUCASS2023-957

of the experiment due to the extreme heating and strong pyrolysis outgassing. The time profiles are separated into three plots; first we show the whole test duration (Fig. 10 (a)), then the first 30 s (Fig. 10 (b)), followed by the last 40 s (Fig. 10 (c)). The emission decreases over test time as pyrolysis strongly progresses and also because the surface front moves away from the spectrometer optical path due to ablation. From 410 s onward, a strong signal can be observed again due to the emission of metallic contributors, possibly coming from both, the degeneration of the titanium liner but also from the internal thermocouples.

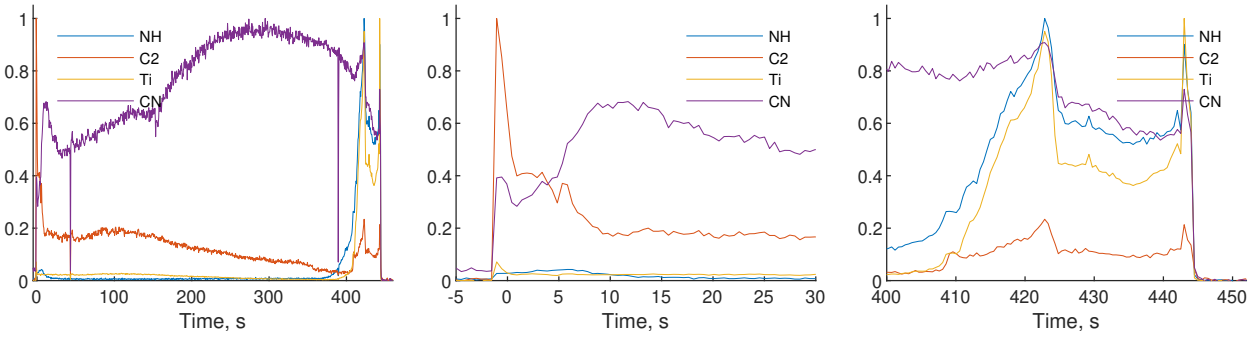

Figure 14: Test 6 temporal OES emission profiles over the whole test time (a), the first 30 s (b), and the last 40 s (c) show the strong emission at test start, mostly due to pyrolysis gas injection into the boundary layer, and the strong decrease during the test (a). Once the titanium liner starts demising, emission strongly rises again (c).

4.4 test 1 and 2, (Stagnation configuration, 55 Pa, 3.7 MW/m^2), test 4 and 5 (Sidways configuration, 55 hPa, 3.1 Mw/m^2),

Test 1 and 2 were conducted with a stagnation configuration, at 55 Pa static pressure and heat flux of 3.7 Mw/m^2. Test 1 had a titanium liner and test 2 had a graphite liner. The test duration varied between both tests, test 1 was subjected to plasma for 94 seconds (conserving the actual reentry heat load, Table 4) while test 2 ran for more than 700 seconds (until demise). It was apparent that minimal damage occurred to test 1 sample after 94 seconds. Furthermore, for test 2 sample, all the carbon wrapping was degraded at the stagnation point. Even though test 2 ran for a very long duration, no through hole was achieved at the stagnation point. The graphite liner maintained its appearance.

For test 4 and 5, 55 hPa static pressure was maintained and heat flux of 3.1 MW/m^2 was used in the sideways configuration. Test 4 had a titanium liner while test 5 had a graphite liner. Test 4 was subjected to plasma stream for 133 seconds (again conserving the actual reentry heat load, Table 4) while test 5 was conducted for 447 seconds (until demise). The carbon wrapping in test 4 remained intact at the stagnation point, with a slight change in colour on the backside. This discolouration could be due to several reactions that occurred with the burning gases. For test 5, similar behaviour to that described previously in test 6 was observed. The majority of the damage was formed between the side carbon wrapping and the surface wrapping. No through-hole was managed by the plasma in the graphite liner at the stagnation point. The surface temperature (FLIR, Pyrometer, and Radiometer) along with thermocouple data was obtained for all 4 tests (Fig. 15). Unfortunately, part of the FLIR data was lost for test 2. The "interrupted" pyro data that is reported for test 1 and test 2 is due to experimental error, a glass window was used, this window has low transmissivity to one of the 2 color pyrometer bands resulting in a higher "apparent" temperature which is above the operating temperature range for the purometer instrument. The window was replaced be a Quartz window for the rest of the campaign. No special or additional character/behaviour was observed for any of these tests compared to what was discussed previously in tests 3 and 6. The temperature trend was similar to that discussed previously for test 3 and 6.

DOI: 10.13009/EUCASS2023-957

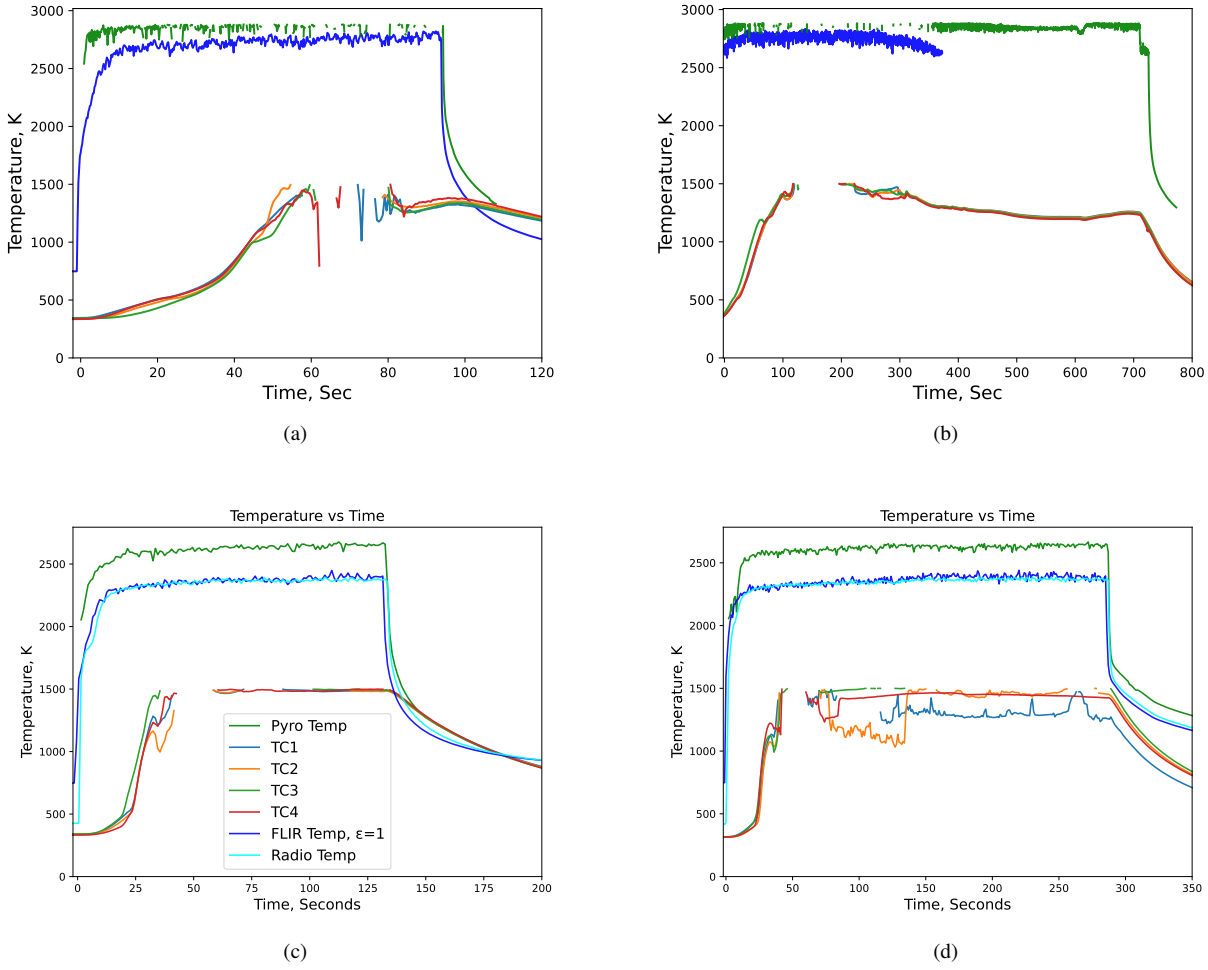

Figure 15: Apparent emissivity independent surface temperature [Kelvin] measured by the Pyrometer, FLIR, and radiometer. For FLIR and Radiometer the emissivity setting =1. The internal temperature recorded by the thermocouples (TC1,TC2,TC3, and TC4) was also reported. a) test 1, b) test 2, c) test 4, d) test 5.

5. Conclusions and perspectives

We conducted an experimental test campaign for an improved understanding of the material performance of Carbon overwrapped pressure vessels on miniaturized test samples with the final goal to perform high-fidelity numerical simulations of those experiments with the ARGO solver (Cenaero), not presented here.

A stagnation point and a sideway configuration were tested, with two of three samples for each configuration with a titanium liner and one with a graphite liner for comparison. All samples were wrapped with carbon fibres. The vessels were subjected to plasma testing under various pressure, heat flux and test duration. Intrusive and non-intrusive techniques were used to obtain the internal temperature, surface temperature and gas emission. Demise (through hole) was achieved with the titanium liner samples. The graphite liner samples survived the test conditions. In both cases, the carbon wrapping degraded away at the stagnation point but stayed intact around the rest of the samples. For the sideways configuration, the damage initiated between the side wrapping and the face wrapping where heat flux is assumed to be the highest at the curvature.

Regarding future analysis, numerical simulations using a unified numerical approach (ARGO), which solves the flow through and around the degrading porous material will be conducted. Volume averaging theory is used to describe the flow through the reactive porous medium macroscopically and derive a single set of equations valid in the whole computational domain. This allows capturing the gas-surface interaction with high accuracy. Furthermore, the emissivity of the material will be determined based on surface radiometry measurements by instrumentation of various spectral ranges.

DOI: 10.13009/EUCASS2023-957

6. Acknowledgements

We acknowledge funding from ESA contract 4000122710/17/NL/KML/fg:
"AblaCCOD: Identification of ablation process in porous materials". Louis Walpot, the technical officer for this work, is acknowledged for his support. Pascal Collin and Terence Boeyen are acknowledged for their help with carrying out the experimental Plasmatron campaign. We acknowledge MOSS Composites, in particular, Stefan van Raemdonck, for the discussions and helpful input in designing and manufacturing the test samples.

References

[1] H. Klinkard. *The hazard of orbital debris, Handbook of cosmic hazards and Planetary Defense*. Springer, 2015.

[2] T. Lips. Engineering models for destruction analysis of spacecraft during re-entry. In *von Karman Lecture Series*, 2016.

[3] D. Riley, I. P. Fuentes, C. Parigini, J.-C. Meyer, P. Leyland, G. Hannemann, E. Guzman, C. Kanesan, and T. Lips. "Design for Demise" Technqiues to reduce re-entry casualty risk. In *66th International Astronautical Congress, Jerusalem, Israel*, 2016.

[4] Joe Benton, Ian Ballinger, Alberto Ferretti, and Niccola Ierardo. Design & manufacture of a high performance high mass efficient gas tank for the vega avum. In *43rd AIAA/ASME/SAE/ASEE Joint Propulsion Conference & Exhibit*, page 5500, 2007.

[5] B Virgili, S Lemmens, J Siminski, and Q Funke. Practicalities of re-entry predictions–the vega-01 avum case. In *7th European Conference on Space Debris*, volume 4, 2017.

[6] Benoit Bottin, Olivier Chazot, Mario Carbonaro, V Van Der Haegen, and S Paris. The vki plasmatron characteristics and performance. Technical report, VON KARMAN INST FOR FLUID DYNAMICS RHODE-SAINT-GENESE (BELGIUM), 2000.

[7] B. Helber, A. Turchi, J. B. Scoggins, A. Hubin, and T. E. Magin. Experimental investigation of ablation and pyrolysis processes of carbon-phenolic ablators in atmospheric entry plasmas. *Int. J. Heat. Mass. Trans.*, 100, 2016.

[8] I. Pontijas Fuentes, D. Bonetti, F. Letterio, G. de Miguel, G. Blanco Arnao, P. Palomo, C. Parigini, S. Lemmens, T. Lips, and R. Kanzler. Upgrade of esa's debris risk assessment and mitigation analysis (drama) tool: Spacecraft entry survival analysis module. *Acta Astronautica*, 158:148–160, 2019.

[9] A Fagnani. Plasma testing methodology for demise phenomena analysis. *Project report, von Karman Institute for Fluid Dynamics*, 2018.